Received: 31 May 2021 | Revised: 16 August 2022 | Accepted: 26 September 2022
DOI: 10.1002/pen.26165

RESEARCH ARTICLE

POLYMER ENGINEERING AND SCIENCE
WILEY

Numerical simulation of poly(lactic acid) polymeric composites reinforced with nanofibrillated cellulose for industrial applications

Edimilson Zambaldi[1] | **Ricardo R. Magalhães**[2] | **Matheus C. Dias**[3] | **Lourival M. Mendes**[3] | **Gustavo H. D. Tonoli**[3]

[1]DSc Biomaterials Engineering, Department of Forest Science, Federal University of Lavras, Lavras, Brazil
[2]Department of Engineering, Federal University of Lavras, Lavras, Brazil
[3]Department of Forest Science, Federal University of Lavras, Lavras, Brazil

Correspondence
Edimilson Zambaldi, DSc Biomaterials Engineering, Department of Forest Science, Federal University of Lavras, Lavras, Brazil.
Email: zambaldibt@gmail.com

Abstract

The advancement of biodegradable polymer application is increasingly growing through various combinations with other materials. There is a great expectation on how the use of those new materials can be expanded not only as a replacement for polymers of fossil origin but also in the replacement of metallic materials. Thus, this work presents the use of numerical simulations as a tool to evaluate and reengineer the application of a biodegradable composite constituted by nanofibrillated cellulose (NFC) and poly(lactic acid) (PLA), in the construction of mechanical components. The academic and industrial interest of this work led to a case study using the finite element analysis (FEA) and the composites produced, where it was evaluated the technical feasibility of replacing a mechanical component constructed with 1060 H12 aluminum alloy.

KEYWORDS

bamboo fibers, biocomposites, finite element analysis (FEA), microfibrillated cellulose (MFC), modeling, polylactic acid

1 | INTRODUCTION

Poly(lactic acid) (PLA) is a biopolymer-based thermoplastic obtained from 100% renewable sources, such as corn sugar and beet sugar. The main limiting factors for the use of PLA are its brittleness and its hydrophobic character for mixing with hydrophilic materials.[1,2] The fracture in this material occurs with a very low elongation, which means low ductility and low toughness, so necessary in various applications. Much research has been carried out with the objective of increasing the toughness of these materials with the use of plasticizers or other polymers and copolymers forming blends and composites, resulting in large losses in mechanical strength.[2–4] Other works aim to minimize this effect by inserting nanomaterials as reinforcement in the PLA matrix. Several works reported the use of nanofibrillated cellulose (NFCs)[5–9]; however, its hydrophilic nature creates an immiscible composite with PLA and, consequently, it results in feeble interface, which limits the transmission of loads in the material macrostructure.

Bamboo is an excellent option to obtain sustainable natural micro or nanofibrils, because, since it is a plant of rapid growth, rich in cellulose, it completes its cycle in a few months and reaches maximum strength in a few years. Interest in those materials arises from a desire to create electronic and mechanical components that are sustainable, biodegradable, and biocompatible.

Evaluating the use of PLA and NFC in the formation of biocomposite materials, with characteristics of mechanical strength that allow the application in mechanical systems is of industrial and academic interest, since industrial components are subjected to stress efforts, considering the possibility of replacing both polymers of fossil origin and non-renewable matrices commonly used, as well as metallic materials, in advanced engineering applications. When a component is subjected to mechanical stresses, the industry has computational methods capable of simulating these stresses before its construction, thus predicting its behavior and possible failures. Through numerical simulation, it is possible to apply the mechanical properties, boundary conditions, and application of loads to the mathematical model of the composite component, in addition to modifying it geometrically or even comparing it, when applying other materials with different characteristics. This strategy shortens the time to put the material for commercialization and may avoid other more expensive testing methods, being possible to apply it for optimization of materials and product design.

2 | MATERIALS AND METHODS

2.1 | Materials

The bamboo used was the *Bambusa vulgaris* sp., from Lavras, Minas Gerais State, Brazil. The region is located at 919 m above sea level and, according to the Koppen and Geiger classification, the climate is humid subtropical (Cwa), with an average annual temperature of 19.9°C and average annual precipitation of 1486 mm. The plant, approximately 3 years old, was cut in the Summer of 2018 and the upper culms were used, which were ground and passed through a 40-mesh sieve (0.42 mm aperture) with a 60-mesh retention (0.25 mm aperture).

The PLA chosen for this research (3251D from NatureWorks) presents a higher melt flow capability, which allows easier molding of thin-walled parts and behaves in a stable way in the molten state. It has high strength and stiffness, with a relative high glass transition temperature (~60°C). Its amorphous structure presents a low degree of crystallinity because its L:D isomer ratio is about 98:2.

2.2 | Alkaline treatment of bamboo particles

Alkaline treatment was performed in 2 consecutive cycles without drying. At each cycle, the material (60 g) was placed under constant mechanical stirring at 600 rpm with 40 ml of 5% NaOH for each 1 g of fiber, for 2 h at 80°C, followed by washing in distilled water until reached pH ~ 7 and finally passed through a 270-mesh sieve.

2.3 | Bleaching process of bamboo fibers

The bleaching treatment was performed in 2 consecutive cycles without drying. At each cycle, the material (60 g) was placed under constant mechanical stirring at 600 rpm, with 40 ml of 1:1 solution (24% H_2O_2 solution: 4% NaOH solution) for each 1 g of material for 3 h at 60°C followed by washing in distilled water until reach pH ~ 7 and finally sieving through 270 mesh.

2.4 | NFCs production by mechanical nanofibrillation

The bleached bamboo fibers were immersed in deionized water at a concentration of 1.5% for 3 days to guarantee the fiber swelling. Afterward, the fibers suspension was subjected to 5 passes in the ultra-fine grinding machine model MKCA6-2 (Masuko Sangyo, Japan), with a distance of 50 μm between the grinding stones, at 1500 rpm and current variation between 3.75 and 4.00 A.[10,11] The result obtained was a colloidal solution of NFCs in gel form. To facilitate mixing in the proper proportions of the masterbatches, drying was carried out by freeze drying in order to avoid agglomerations in the material. For this, a Buchi machine model L200 was used with a freeze-drying cycle at a controlled freezing rate of 50°C/h to −40°C. After freezing, a vacuum was created (P = 0.086 mbar) and a first heating cycle with the rate of 5°C/h until reaching −5°C. Then, a second heating cycle started with a rate of 3°C/h until reaching 20°C. Figure 1 shows the flowchart to obtain dehydrated NFCs as described, with the physical aspects of each step.

2.5 | Morphological properties of NFCs by transmission electron microscopy (TEM)

The morphology of the CNFs was investigated using a Tecnai G2-12 (FEI company) instrument with an accelerated voltage of 80 kV. Sample preparation and TEM configurations followed recommendations described elsewhere.[12] Diameter measurements of CNFs were performed for at least 300 individual structures per image using open-source software biological image analysis Fiji.[13]

FIGURE 1 Flowchart to obtain the cellulose nanofibrils (NFCs) from bamboo culms

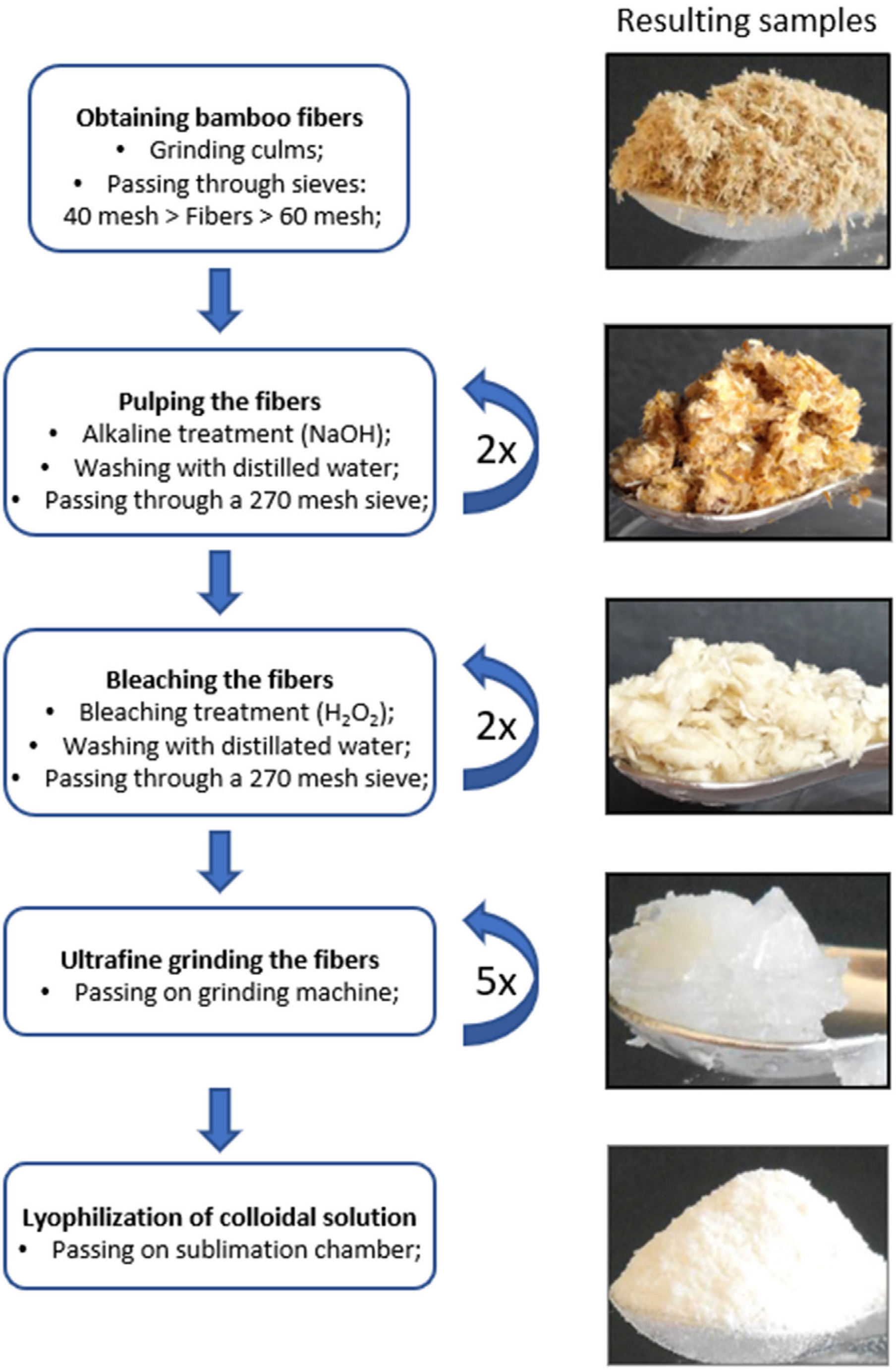

2.6 | X-Ray diffraction (XRD) analysis of NFCs

The XRD analyzes were performed using a PANalytical X'Pert PRO MPD X-ray diffractometer (Malvern Panalytical, UK), equipped with an X'celerator detector with a Cu-Kα source ($\lambda = 0.15406$ nm) in the 2θ range of 10–40°. A step rate of 0.066° was used. The equipment was operated at a tension of 45 kV and a current of 40 mA.

The patterns were deconvoluted with the software Magic Plot 2.9 (Magicplot Systems, Russia). For the amorphous halo, cellulose II pattern with $\text{FWHM} = 9$, only varying its intensity, was used as suggested in the literature.[14] After deconvolution, the crystalline fraction (CF) was calculated from the ratio between the area below all the crystalline peaks and the total area (area of crystalline peaks + area of amorphous halo) below the whole curve, determined after deconvolution following Equation (1):

$$\mathrm{CF}(\%) = \frac{\sum \mathrm{Area}_{\text{Crystalline Peaks}}}{\sum \mathrm{Area}_{\text{Crystalline Peaks}} + \mathrm{Area}_{\text{Amorphous Halo}}} \tag{1}$$

2.7 | Production of PLA/NFCs composites

PLA composites were produced with NFCs reinforcement concentrations of 30%, 40%, and 50% of their weight (wt %) and with the use of glycerol G5516, supplied by the company Sigma-Aldrich, as a plasticizer, in the proportion of 4% and 6% of the total weight. The quantities were weighed and reserved using a Sartorius Analytical model Entris and each master batch was processed using FKV 3L reactor, double glazed, with an oil bath at 60°C, under vacuum and mechanical stirring at 150 rpm. Then, the PLA was placed in the reactor with deionized water in the proportion of 5:1 of the volume for 20 min for the best dispersion of the glycerol, which was inserted in a second phase and remained in the same stirring conditions for an additional 20 min for complete homogenization. In a third step, the volume of NFC was slowly inserted into the still moist mixture. The material remained under mechanical stirring in the same conditions for an additional 80 min.

Several specimens of composites were created, including those made of neat PLA used for comparison. These proportions were determined based on theoretical references and previous works,[15–24] according to the desired mechanical properties for the purpose of this work, in order to obtain a material with the maximum plastic deformation without great loss in strength, as a consequence of the increase in toughness.

The molding was used to obtain the specimens in type I standard, for the tensile strength (TS) test (ASTM D638, 2014) and in type IA for the notched IZOD impact (IS) test (UNI EN ISO 180, 2001; ASTM D256, 2010), in the quantity of 4 units per test and per composite treatment. For this, the masterbatches of each composite were extruded and pelletized in the form of granules with maximum dimension of 2 mm, using an extruder with BPM pelletizer model SB100 with 50 rpm double screw extruder speed. The pelleted granules were left to rest in a dry room for 24 h and, before being placed in the injection funnel, returned to the oven and remained for 10 h at a temperature of 60°C and, right afterward, injected in specific double molds using an Arburg model 370E injector with a speed of 10 cm/s. Pressure and settlement time during injection was 10 bar and 10 s. The mold was preheated to 80°C with a cooling time of 10 min. Thus, the specimens for each sample treatment were created and received a designation as shown in Table 1.

TABLE 1 Designation and the proportions (wt%) of the raw materials for each treatment sample.

Sample treatments	PLA (%)	NFC (%)	Glycerol (%)
Neat PLA	100.0	0.0	0.0
PLANFC30/4	67.2	28.8	4.0
PLANFC30/6	65.8	28.2	6.0
PLANFC40/4	57.6	38.4	4.0
PLANFC40/6	56.4	37.6	6.0
PLANFC50/4	48.0	48.0	4.0
PLANFC50/6	47.0	47.0	6.0

2.8 | Thermal tests and mechanical properties

After specimens were prepared, they were measured and weighed to establish their densities and the cross-section for the tests. The first test performed was the TS test, to provide the stress–strain curves from each material. For this, a universal testing machine Zwick Z010 with a full scale of 10 kN was used. The test was performed with 50 mm/min of traverse movement speed in a room with the temperature set to 21°C and 55% of relative humidity. The minimum characteristics expected for the materials using this method are modulus of elasticity of about 3.0 GPa and minimum elongation at break of around 7%.

The DSC test was performed for neat PLA and composites, in a Linseis STA PT-1000 instrument, following the UNI EN ISO 11357-32 (ASTM D3418) standard, with samples of around 12 and 15 mg, heated at a rate of 10°C/min in the range from 25°C to 250°C in a hermetic box with nitrogen as a carrier gas in constant flow of 50 ml/min, in order to measure the amount of energy needed to establish the thermal balance using inert material as reference. The degree of crystallinity (X_c) of the sample treatments was estimated using the specimen enthalpy of fusion.[23]

The IS test was performed according to UNI EN ISO 180 (ASTM D256) standard using Zwick equipment, model HIT25P, 25 J (3.8 m/s) of full scale at room temperature (~22°C). The "V" notch in the specimens must be performed after molding to avoid the stress concentrations during injection and solidification. For this purpose, a JT Tohsi notching tool type TVH 603 was used.

2.9 | Finite element analysis (FEA) for mechanical stress

To evaluate the material properties in the mathematical model, the FEA was performed for the three composite treatments chosen with higher elongation at break and without great loss of strength, along with the neat PLA used as control sample. Thus, the drawing of specimen models and their respective simulations were carried out in the commercial software SolidWorks, which can perform finite element analysis (FEA) with a certain precision. For each material, the stress–strain curve was loaded, and the material properties were applied, according to previous experimental tests and measurements. This procedure was done to verify if the 3D model simulation results matched the values obtained in the physical tests. Previously, a 3D model mesh analysis convergence was performed. For this, meshes were created on the model, reducing the distance among nodes, and the strength of the materials was controlled on a reference node, one at a time for each simulation until stabilization was achieved. By applying this procedure, it was possible to use the same meshing parameters to reproduce the test for each sample treatment and compare results from simulations and real physical/mechanical tests. In this case, the boundary conditions were replicated in the model as found in the experimental tests, the load applied accounted for 80% of strength yield (limit of proportionality-LOP) for each material, and the strength values (von Mises stress) were registered at a reference point. This procedure was performed decreasing the distance between nodes until the convergence of the strength values was reached.

Therefore, the convergence analysis is required for all FEAs in order to reach accurate results using minimal computation resources. Refinements were used to reduce error of approximation of the finite element model, which are ways of increasing the degrees of freedom of the elements in a model, to reduce error of discretization in subsequent mesh convergences, applying different forms of elements, other than triangular, such as follows: quadrilateral, tetrahedral, hexahedral.[25–27]

The choice of material for a specific application must, initially, consider the intensity of the active stresses. Therefore, it is necessary to seek bases or criteria that allow such a judgment to be made. There are several failure criteria, and their use relies largely on how the material absorbs deformation in a fragile or ductile way, i.e.; Mohr, Rankine, von Mises, and Tresca. The von Mises criterion, for example, would be an evolution of the Tresca criterion for ductile materials, which are based on the shear stress as the cause of the material failure, a phenomenon easily observed in experimental uniaxial tensile tests on steel bars, where the failure occurs with plane displacement with a 45° inclination of the axis of load application, where the stress is maximum. The von Mises criteria consider the shape variation with constant volume, also based on experimental evidence from the tensile test, but declare that the flow of a material occurs when the distortion energy per unit volume of the material is equal to or greater than the energy of distortion per unit volume of the same material when it reaches the flow in a tensile test, which is represented by Equation (2).[28,29]

$$\sigma_{\mathrm{vonMises}} = \sqrt{\frac{(Sx-Sy)^2+(Sx-Sz)^2+(Sy-Sz)^2+6\left(Txy^2+Txz^2+Tyz^2\right)}{2}} \tag{2}$$

where: Sx is the normal strength on x-direction; Sy is the normal strength on y-direction; Sz is the normal strength on z-direction; Txy is the shear strength in y-direction (YZ plane); Txz is the shear strength in z-direction (YZ plane); Tyz is the shear strength in z-direction (XZ plane), Tyx is the shear strength in x-direction (XZ plane), Tzy is the shear strength in y-direction (XY plane) and Tzx is the shear strength in x-direction (XY plane).

Since the mesh quality is fundamental to the result accuracy, the software application uses two checks to assess the quality of the elements within the mesh: checking of proportion and Jacobian points. In case of a solid mesh, better precision is achieved with the dimensional uniformity of the elements, that is, elements with the same length as the edges, which find deformations during their formation in areas with small edges, curved geometries, and pronounced corners. The proportion check controls the variation between edges of the deformed elements with the variation that in theory is perfect; therefore, the proportion is defined as the ratio between the longest and the shortest normal, relative to a vertex opposite to the normalized face of a perfect tetrahedron. The Jacobian point verification is based on several points drawn within each element. The software application currently provides Jacobian verification at 4, 16, and 29 Gaussian points or at nodes. The intermediate nodes created at the boundary edges of an element

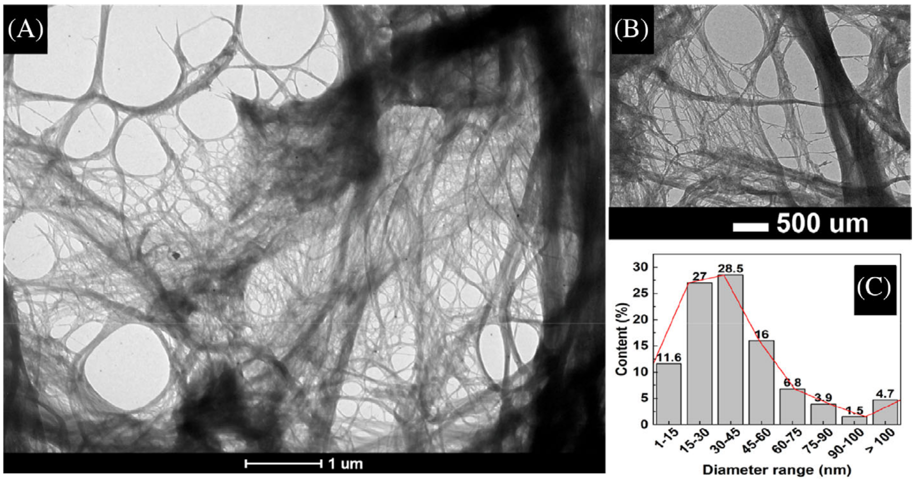

FIGURE 2 Typical transmission electron microscopy (TEM) images of the bamboo NFCs: (A) NFC network overview; (B) more detailed observation of the fibril network of bamboo NFCs; and (C) diameter distribution of the bamboo NFCs

are placed in the real geometry of the model. At very pronounced or curved limits, these additions of nodes can cause the generation of distorted elements with invading edges, which returns a negative Jacobian matrix value for this element and, consequently, the software application indicates an error in the mesh formation. The greater the number of Jacobian points, the greater precision will be required in the construction of the mesh. The calculation time is directly proportional to the number of nodes and degrees of freedom that were determined for the mesh construction and depends mainly on the complexity of the model geometry, its volume, and the boundary conditions involved. The result appears in the form of the geometric model, where the elements are replaced with the chromatic gradient of stress distribution in all regions of the mathematical model.

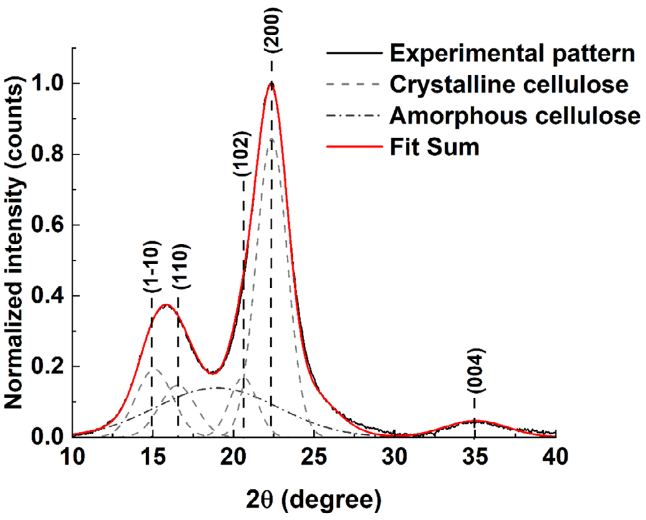

FIGURE 3 Typical XRD pattern of the bamboo NFCs

3 | RESULTS AND DISCUSSION

3.1 | Morphological properties of bamboo NFCs

Figure 2A, B depicts TEM images of the bamboo NFCs obtained after five passes through the mechanical nanofibrillator, respectively. The mechanical disruption caused by nanofibrillation resulted in fibrillar structures with lengths estimated at thousands of nanometers and diameters predominantly smaller than 100 nm.

Figure 2A, B also show that 5 passes in the mechanical nanofibrillation equipment were sufficient to efficiently deconstruct the cell wall of the bamboo fibers, releasing and individualizing the nanofibrils, producing structures with an average diameter of 42 ± 29 nm. Bamboo NFCs are predominantly in the diameter range between 15 and 45 nm (Figure 2C), representing ~56% of the measured structures. This result agrees with what is found in the literature for bamboo NFCs[30] and for wood NFCs, such as pine and eucalyptus, both bleached and unbleached.[10,11]

Furthermore, the NFCs suspension presented around 39% of nanofibrils with a diameter between 1 and 30 nm (Figure 2C). According to Tonoli et al.,[31] NFCs in this range of dimensions make them potentially useful as reinforcing agents in composites. Figure 2C further shows that around 95% of all measured structures had diameters between 1 and 100 nm. According to Siró and Plackett,[32] for a material to be considered a nanomaterial, at least one of its dimensions must be in the nanometer range (1–100 nm).

3.2 | XRD analysis

X-ray diffraction (XRD) pattern of Bamboo NFCs is shown in Figure 3. These patterns are typical for

TABLE 2 Average and SD values of the properties determined by tensile testing, highlighting the three best composites selected by higher values of elongation at break (Eb) and modulus of elasticity (MOE)[a]

Sample treatments	Section (mm^2)	TS (MPa)	MOE (GPa)	Eb (%)	υ	Ds (g/cm^3)
Neat PLA	39.95	60.9 ± 2.2	3.3 ± 0.1	3.8 ± 0.2	0.31 ± 0.01	1.26 ± 0.01
PLANFC30/4	39.88	55.2 ± 1.8	2.9 ± 0.1	6.3 ± 0.3	0.32 ± 0.01	1.27 ± 0.01
PLANFC30/6	39.92	54.8 ± 1.9	2.9 ± 0.1	6.7 ± 0.3	0.33 ± 0.01	1.27 ± 0.01
PLANFC40/4	39.98	56.1 ± 2.3	**3.2 ± 0.1**	**7.4 ± 0.3**	0.33 ± 0.01	1.28 ± 0.01
PLANFC40/6	39.92	55.5 ± 2.1	**3.2 ± 0.1**	**7.6 ± 0.3**	0.34 ± 0.01	1.28 ± 0.01
PLANFC50/4	39.96	59.5 ± 2.8	**3.2 ± 0.1**	**6.9 ± 0.5**	0.33 ± 0.01	1.28 ± 0.01
PLANFC50/6	39.93	58.9 ± 2.9	3.1 ± 0.1	6.8 ± 0.4	0.33 ± 0.01	0.01

[a] υ, Poisson's ratio; Ds, Apparent density; Eb, Elongation at break; MOE, Modulus of elasticity; TS, Tensile strength.

semicrystalline materials with amorphous halo and crystalline peaks. The sample presented the typical parallel crystalline structure of cellulose Iβ with peaks at 2θ = 14.9°, 16.4°, 20.5°, 22.6, and 34.7°, corresponding to lattice planes (1–10), (110), (102), (200) and (004), respectively.[33] The XRD patterns show a sharp peak near to 2θ = 22.6°, which can be attributed to the (200) lattice plane of cellulose I. The cellulose CF is directly dependent on the area of the crystalline peaks, being also inversely proportional to the amorphous halo. Small peaks close to 2θ = 20.4° relative to the plane (102) were observable through the deconvolution technique, which demonstrated that there was no preferential orientation of the cellulose crystals.[34]

A CF of 67 ± 2% was calculated using the deconvolution method, a value in accordance with what is found in other works in the literature.[30,35] It shows that the material has high crystallinity, which could improve the TS and elastic modulus of other materials, making it interesting to use these NFCs as a mechanical reinforcement agent in composite materials.[36,37]

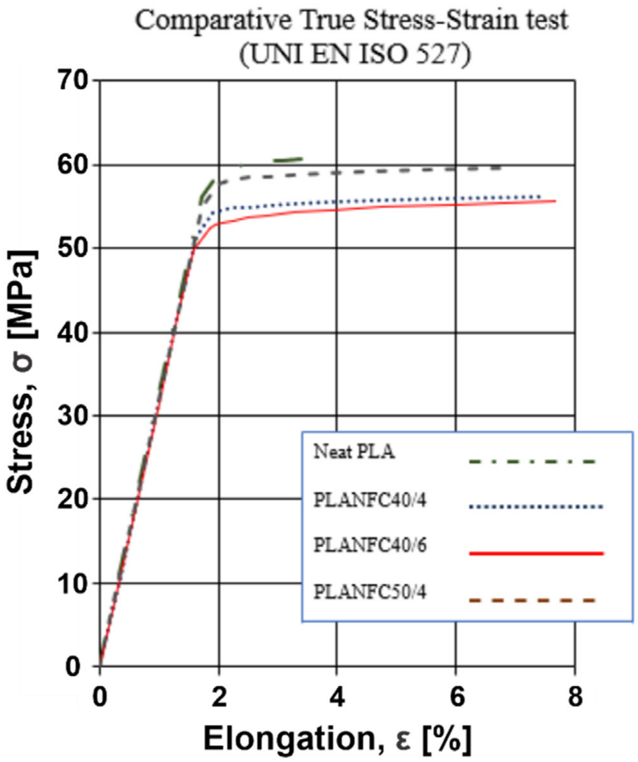

FIGURE 4 Typical stress-elongation curves of the selected composite treatments

3.3 | PLA/NFCs composites properties

The key processes for obtaining homogeneous specimens of the composites here were as follows: (i) avoid the agglomeration of NFCs throughout the process; (ii) improve their dispersion in the PLA, and (iii) control temperatures during extrusion and injection of the composites. For temperature control, the goal was to keep the temperature high enough for the low viscosity of the PLA, improving dispersion conditions of the NFCs and maintaining good composite flow during extrusion and injection, but at the same time ensuring the temperature would not get too high, to avoid degradation of both PLA and NFCs. The heat slightly changed the material color to a darker shade, but the visual result was homogeneous. The cooling in the mold, at a rate of 6°C/min, aimed to inhibit the formation of micro cracks and undesirable change of the material crystallinity degree. The mean values of TS, modulus of elasticity, elongation at break, Poisson's ratio, and apparent density for each composite are shown in Table 2.

PLANFC40/6 showed a better ratio of elongation at break to the modulus of elasticity, compared to neat PLA and other composites. This ratio of resistance to

TABLE 3 Average and SD values for Izod impact test and main results of DSC test[a]

Sample treatments	IS (kJ/m^2)	Tg (°C)	Tm (°C)	Xc (%)
Neat PLA	6.4 ± 0.8	61.1	189.2	3.6
PLANFC30/4	10.0 ± 1.3	64.3	168.5	11.3
PLANFC30/6	10.1 ± 1.2	63.4	162.8	10.2
PLANFC40/4	11.2 ± 1.4	63.1	166.3	13.4
PLANFC40/6	11.6 ± 1.6	62.5	163.8	12.7
PLANFC50/4	10.1 ± 1.8	64.3	166.0	11.9
PLANFC50/6	10.0 ± 1.9	63.8	165.4	13.3

[a] IS, Impact strength; Tg, Glass transition temperature; Tm, Melting temperature; Xc, Degree of crystallinity.

elongation is explained because, in addition to the material resistance to deforming elastically, signaled mainly by the high modulus of elasticity, it is expected that this material is also not as brittle and reacts well to impact efforts, in case of collision. Therefore, material elongation is also important, as it is a good indicator of the increase in toughness, which can be confirmed by the IS test. The material is expected to be able to absorb a great deal of energy both in the elastic phase and in the plastic phase before fracture. When comparing PLANFC40/6 with neat PLA, there was an approximate decrease of around 3% for MOE, a decrease of around 9% for TS and an increase of around 101% for elongation at break (Eb), which corresponds to the increase of its toughness. Figure 4 shows the stress–strain curves of the sample treatments selected (highlighted) in Table 2.

Table 3 presents the main values for the DSC analysis and the Izod impact tests. A greater proportion of the reinforcement (NFC) slightly increases glass transition temperature in relation to neat PLA, and a greater proportion of the plasticizing agent tends to lower it. On the other hand, the melting temperature decreased when using NFC (a difference of 26.4°C for the PLANFC30/6 composite compared to neat PLA). Also, in Table 3, there is an increase of the impact resistance (IS) values based on the proportion of the reinforcement and the plasticizer; this increase reached its maximum value in the PLANFC40/6 composite (~81% higher than neat PLA). The increase in the composite degree of crystallinity is due to the addition of the reinforcement phase (NFC), given the PLA used in this work, basically formed by L-enantiomer (PLLA), is known to be amorphous.

The stress–strain curves from materials PLANFC40/4, PLANNFC40/6, PLANFC50/4, and also neat PLA (as reference) were inserted in Solidworks software application as new materials and linked with their respective 3D model. Furthermore, the information on apparent density and Poisson's ratio for each material was uploaded, obtained from the previous tests and measurements. After that, it was possible to start with the meshing constructions for the 3D model and define the optimal strategy using the meshing parameters.

The commercial software SolidWorks has an internal algorithm that, based on the geometry and volume of the component to be analyzed, automatically presents initial values for mesh parameters. However, the mesh convergence method was followed using the distance between vertices nodes as a progressive mesh thinning process to obtain convergence. Once the reference point in the geometry was defined, for each simulation, distance values between the smallest nodes were followed, starting from 10 mm with decreases of 0.5 mm, with the corresponding stress values recorded on a spreadsheet. It is worth noting that, in various simulations, stress values show great variations, sometimes more and sometimes less, keeping the values of the boundary conditions unchanged, until, with progressive thinning, they reach an acceptable deviation. In this process, the boundary or material conditions do not change the results of mesh convergence, as there is a ratio of the model geometry to volume and how the elements fill the model, and for more complex shapes this convergence requires a smaller distance between vertices nodes and, therefore, a greater number of elements and nodes. In this phase, only second-order tetrahedral elements were used. Values obtained during mesh convergence are shown in Figure 5, where it was observed that the convergence followed with the distance between vertices nodes around 2 mm.

For low-ductile materials observed, the von Mises condition in static simulations is in general the closest to the experimental data. There are other cases, however, in which the Tresca conditions seem to show better correspondence, for example, when the material undergoes plastic deformation even with a constant value for the load (within its limit). Thus, the two methods can be considered useful. For the uniaxial stress states, the two criteria are equivalent, and in cases where the load conditions are the same in multiaxial stress states, the Tresca criterion led to greater plastic deformation compared to the von Mises criterion, as the former is more conservative. The maximum deviation between the two models occurs for the state of pure shear. In this state of tension, based on the Tresca criterion, the failure occurs at around 87% of the von Mises stress value. Figure 6 shows the specimen simulation for the PLANFC40/6 composite, with the higher stress in the indicated area (in red) at the LOP (~52 MPa). In this case, for a better visualization of the stress distribution in the material, the von Mises stress range was limited to ~27 MPa as the minimum and ~56 MPa as the material rupture stress.

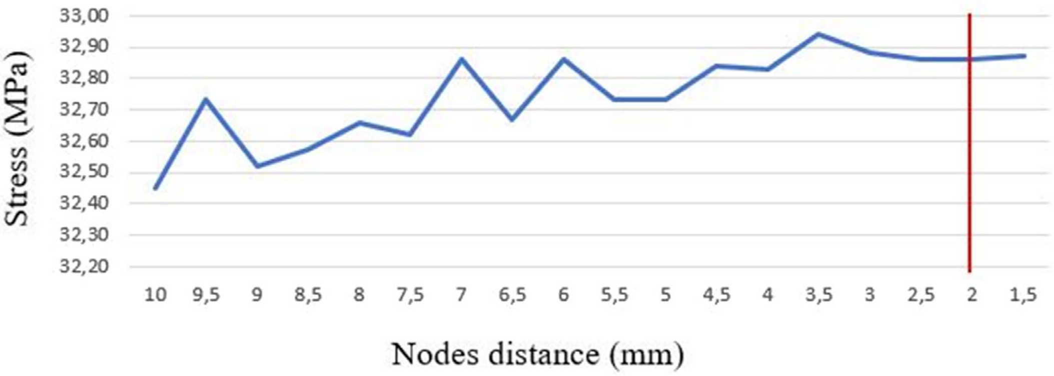

FIGURE 5 Meshing convergence to specimen simulation for PLANFC40/6 treatment

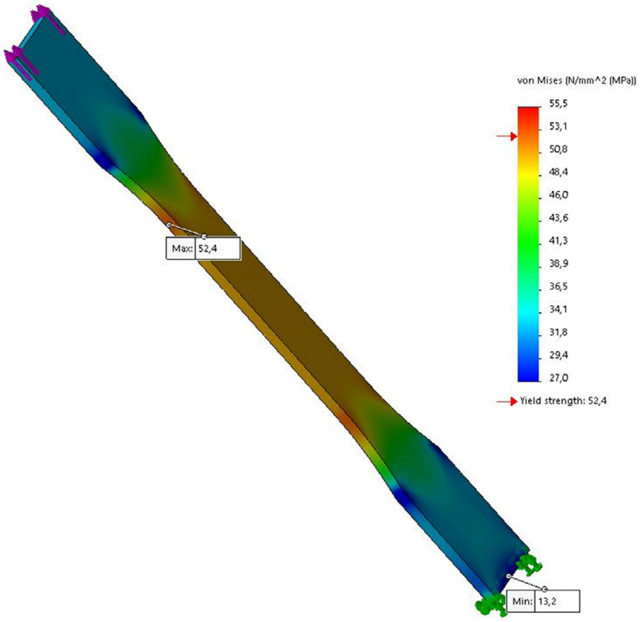

FIGURE 6 Distribution of von Mises stresses in the simulation for the PLANFC40/6 specimen, with the higher stress in the indicated area (in red) at the LOP (~52 MPa)

3.4 | Case study

The objective of this case study was to evaluate and verify the practical application of a PLA/NFC composite to replace a mechanical component, produced in aluminum alloy 1060 H12, based on simulations using FEA. In this case, two equal mechanical components, produced in aluminum alloy 1060 H12, serve as a reaction to the opening of a system of double claws of a gripper, in a tool that is attached to the wrist of a robot (Figure 7). The material is expected to withstand 1500 N of force (value added with a safety factor of 1.5) in each operation to pick, place and support two pins inserted in two labels against a steel bar, while they are welded in a double labeling process.

The first analysis was performed to understand the working temperature at which the part would be submitted since polymers have a much lower melting temperature than metals and may show a viscoelastic behavior starting at the glass transition temperature. For this purpose, a temperature sensor (thermocouple type k) was placed close to the robot tool component in order to record temperatures during operations, which were in the range of 10 to 50°C. Additionally, it was necessary to make sure the component had no contact with substances or environments that could modify its properties or accelerate degradation. After that, the procedure for FEA started with a 3D model of the component reproducing the one in aluminum alloy currently in use. Then, meshing parameters setup, meshing convergence procedures and continuous simulations with several different node distances were performed, in order to get convergence of the stress value in the point chosen as reference.

Before simulating with the composite that showed the best ratio of elongation at break to modulus of elasticity, PLANCF40/6, a simulation was performed with the current aluminum alloy in use, with the meshing parameter set with tetrahedral element (second order) and the distance among nodes of 1.5 mm, as determined during meshing convergence procedure. Figure 8 shows the result of the simulation, confirming the capacity of the material to withstand the load because the yield strength (LOP = 75 MPa) is higher than the maximum stress found (~53.4 MPa).

Figure 9 shows the result of the simulation using the PLANFC40/6 composite as material, where possible failure zones were found (in red). In fact, the simulation with the load induced a stress area of around 69 MPa, which means plastic deformation due to the composite yield strength (LOP) of 52.4 MPa.

A possible change of screws was evaluated as an alternative solution, that is, changing the type of screws to obtain a higher recess that does not cause a concentration of stresses in those areas of possible failure (in red in Figure 9). The preceding aluminum component used M6 screws with cylindrical heads (DIN EN ISO 4762: 2004), and the alternative to be tested would be to replace them with a countersunk M6 screw (DIN EN ISO 10642: 2007).

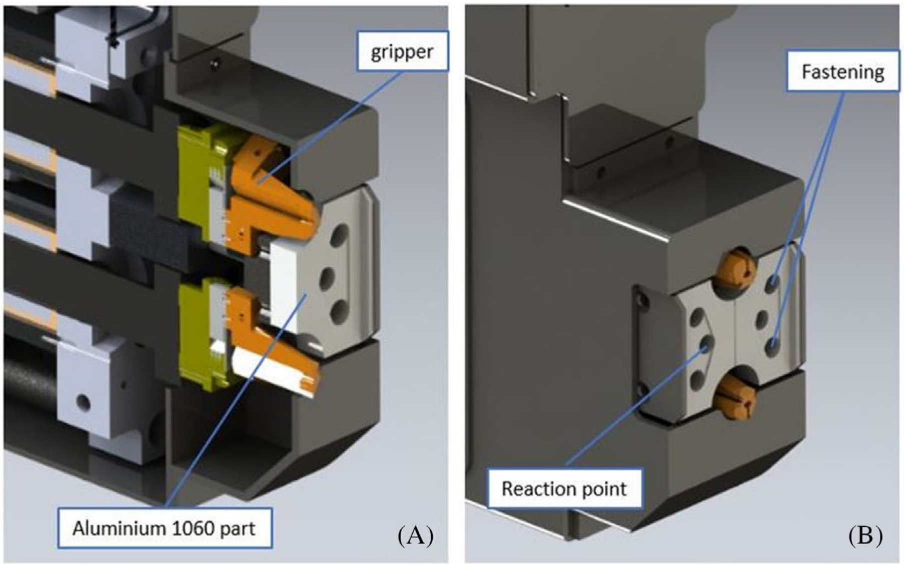

FIGURE 7 Positioning of parts on the robot tool: (A) section of tool with gripper systems; (B) reaction components, area of fastening to the tool, and area behind which the grippers find a reaction

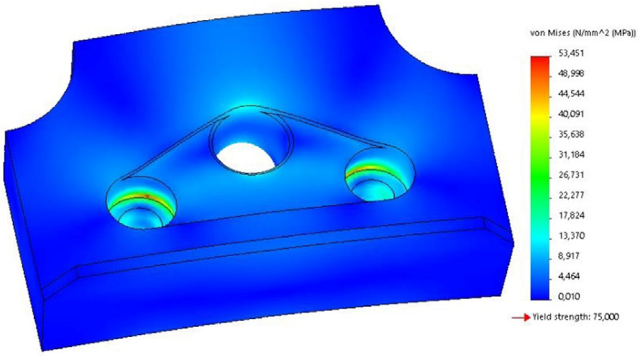

FIGURE 8 Result of simulation using the current 1060 H12 aluminum alloy in use

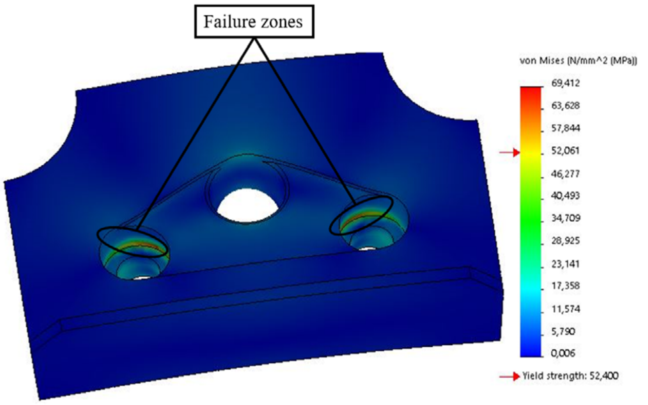

FIGURE 9 Result of simulation using the PLANFC40/6 composite as material. In red are possible failure zones due to stress.

Hence, the 3D model was modified, and new simulation was performed (Figure 10).

This simple component modification using FEA shows the viability to use the composite material in this component because the maximum stress found (~49.9 MPa) is lower than the yield strength of the composite (52.4 MPa). Figure 11 shows, in sections, the difference between the screw heads.

As shown in Figure 11A, when using cylindrical head screws, the material thickness continues absorbing the stresses of 7 mm, whereas, with the use of countersunk screws (Figure 11B), the thickness goes up to 10 mm. In addition to that, the countersunk screw has a 45° inclined angle, rather than the sharp corner caused by the cylindrical counterbore.

Based on the simulations, a component was machined from a rough block of the composite PLANFC40/6 using the countersunk machining as housing for the M6 screw heads. In the machining process, cutting parameters close to polyvinyl chloride (PVC) were used: spindle speed of 6000 rpm, feed rate of 2200 mm/min, double helical milling cutter in HSS (high speed steel), with the use of coolant, resulting in a good finish.[29,38,39] After that, the component was mounted on the robot tool in place of the original aluminum component, keeping the other components unchanged. Then, the robot tool system was subjected to approximately 650 working cycles without showing any type of remarkable change. The component constructed with the produced composite PLANFC40/6 was disassembled after the 650 working cycles for visual assessment and is shown in Figure 12.

A fundamental issue in the application of composites in robot tool components is the relationship between load capacity and their radius of action, that is, a greater radius of action compromises the maximum weight that

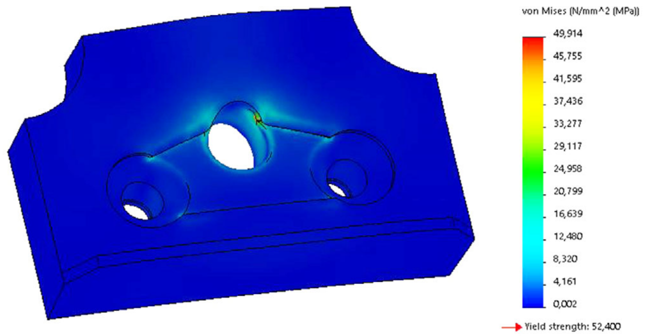

FIGURE 10 Result of simulation using the PLANFC40/6 composite as material with countersunk instead of counterbore hole

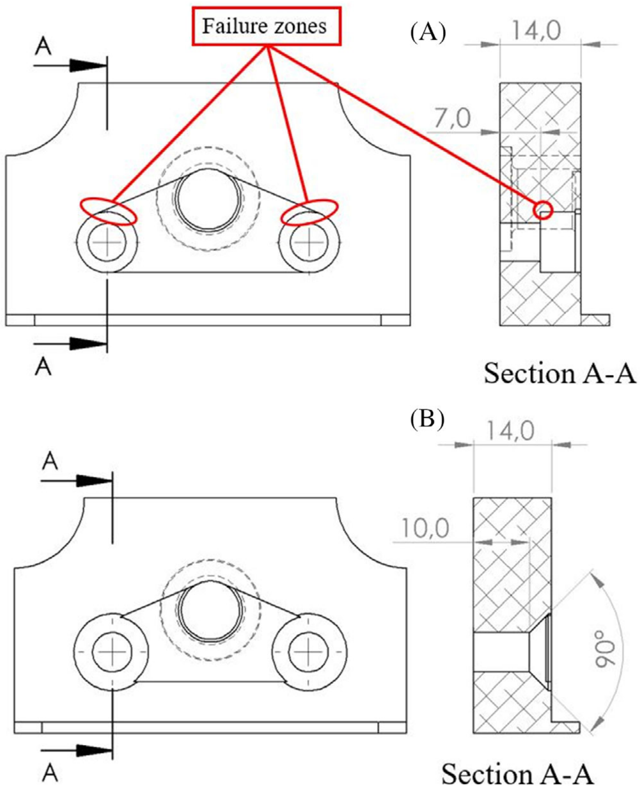

FIGURE 11 Section view with shape of screw heads: (A) counterbore screw section of the component currently in use; (B) section of the alternative countersunk screw

the robot component can support for the tool on its wrist. Therefore, the payload is influenced not only by the total weight of the tool but also by the distance from its barycenter to the robot wrist. The greater this distance, the lower the payload capacity, which is easily verified in the technical data sheets of each robot model. Therefore, it is very important to use lightweight components in the robot working tools. The aluminum parts, which weigh around 161 g, can be replaced with those of the PLANFC40/6 composite, which weigh around 76 g. This can be considered a significant advantage in terms of weight reduction, considering that the apparent density of the PLANFC40/6 composite is 1.28 g/cm^3, whereas the aluminum alloy 1060 H12 is 2.71 g/cm^3. Another benefit noteworthy in this substitution is the dielectric strength of the PLANFC40/6 composite, which is considered insulating, in terms of the electric current that passes through the clamp and transmits to the pin during welding. Thus, it exempts the electrical insulation between the clamp and the component, which is necessary for the aluminum alloy component, as it is an electrical conductor.

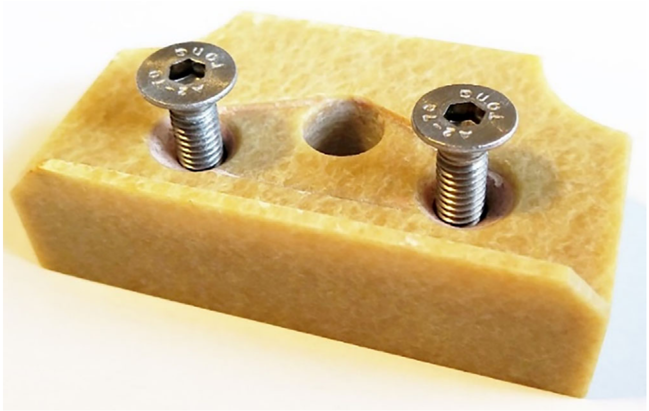

FIGURE 12 Robot component produced with the PLANFC40/6 composite, after around 650 working cycles with countersunk screws

4 | CONCLUSION

This work proposed a biocomposite as alternative to polymers of fossil origin, which are widely used today and can replace, in some cases, metallic materials. This work presented a case study using numerical simulation to evaluate robot tool components produced using these composites, and showed how important this technique is to evaluate, modify and support decision-making through simulations of FEA, avoiding additional costs. It was possible to verify the difference between the results of a simulation of the tensile test and the real physical/mechanical tests, to numerically simulate the model behavior of a mechanical robot component before its production. The composites presented high specific modulus, which is the ratio of modulus of elasticity to weight. The addition of NFC to the composites increased elongation at break and impact strength (IS) in relation to neat PLA. The best formulation defined in physical/mechanical tests and FEA simulations was used to produce a robot tools component. Additionally, through numerical simulations, it was possible to find alternatives in the robot component geometry, which technically enabled the use of the PLANFC40/6 biocomposite to replace the aluminum alloy 1060 H12. This work was limited to considering the composites developed as isotropic materials, inferred by the low degree of crystallinity, which must be further investigated through new tests using specimens, at least, in the other two orthonormal directions. Also, this work was limited to material properties evaluated under a working temperature below glass transition temperature (~63°C) and without a fatigue test, which would determine the material limit based on cyclic stresses.

ACKNOWLEDGMENTS

This work was supported by Federal University of Lavras (UFLA), Rede Religar (Brazil), CAPES, CNPq (Process n.314203/2018-4), and FAPEMIG (Process n. CAG APQ-03248-17).

DATA AVAILABILITY STATEMENT

The data that support the findings of this study are available from the corresponding author upon reasonable request.

ORCID

Edimilson Zambaldi https://orcid.org/0000-0002-5001-3438

REFERENCES

[1] A. C. C. Arantes, L. E. Silva, D. F. Wood, C. G. Almeida, G. H. D. Tonoli, J. E. Oliveira, J. P. Silva, T. G. Williams, W. J. Orts, M. L. Bianchi, *Carbohydr. Polym.* **2019**, *207*, 100.
[2] L. Xu, J. Zhao, S. Qian, X. Zhu, J. Takahashi, *Compos. Sci. Technol.* **2021**, *203*, 108613.
[3] H. Long, Z. Wu, Q. Dong, Y. Shen, W. Zhou, Y. Luo, C. Zhang, X. Dong, *Polym. Eng. Sci.* **2019**, *59*(s2), E247.
[4] N. Saba, M. Jawaid, *Composites* **2017**, *4*, 89.
[5] A. Abdulkhami, J. Hosseinzadeh, S. Dadashi, M. Mousavi, *Cellul. Chem. Technol.* **2015**, *49*(7–8), 597.
[6] E. Rudnik, Compostable polymer materials—Definitions, structures and methods of separation. in *Compostable Polymer Materials [S.I.]*, Elsevier, Oxford **2016**.
[7] S. Ghasemi, R. Behrooz, I. Ghasemi, R. S. Yassar, F. Long, *J. Thermoplast. Compos. Mater.* **2017**, *31*, 1.
[8] M. Ramachandran, R. Bhargava, P. Raichurkar, *Int. J. Textile Eng. Process.* **2016**, *2*, 59.
[9] K. Okubo, T. Fujii, E. T. Thostenson, *Compos. Part A* **2009**, *40*, 469.
[10] M. C. Dias, M. C. Mendonça, R. A. P. Damásio, U. L. Zidanes, F. A. Mori, S. R. Ferreira, G. H. D. Tonoli, *Holzforschung* **2019**, *73*, 1035.
[11] M. C. Dias, M. N. Belgacem, J. V. de Resende, M. A. Martins, R. A. P. Damásio, G. H. D. Tonoli, S. R. Ferreira, *Int. J. Biol. Macromol.* **2022**, *209*, 413.
[12] L. C. E. da Silva, A. Cassago, L. C. Battirola, M. C. Gonçalves, R. V. Portugal, *Cellulose* **2020**, *27*, 5435.
[13] J. Schindelin, I. Arganda-Carreras, E. Frise, V. Kaynig, M. Longair, T. Pietzsch, S. Preibisch, C. Rueden, S. Saalfeld, B. Schmid, J. Y. Tinevez, D. J. White, V. Hartenstein, K. Eliceiri, P. Tomancak, A. Cardona, *Nat. Methods* **2012**, *9*, 676.
[14] A. D. French, *Cellulose* **2020**, *27*, 5445.
[15] T. C. Mokhena, J. Sefadi, E. Sadiku, M. Mochane, A. Mtibe, *Polymer* **2018**, *10*(1363), 1.
[16] T. Ambone, A. Torris, K. Shanmuganathan, *Polym. Eng. Sci.* **2020**, *60*(8), 1842.
[17] A. Sharma, M. Thakur, M. Bhattacharya, T. Mandal, S. Goswami, *Biotechnol. Rep.*, *21*, **2019**, 1.
[18] A. Morales, A. Guenes, A. Lpoez, V. Valero, S. Llano, *Materials* **2017**, *10*(11).
[19] S. Faust, J. Foerster, M. Lindner, M. Schmid, *Polym. Eng. Sci.* **2022**, *62*(1), 95.
[20] Y. Liu, H. Wei, Z. Wang, Q. Li, N. Tian, *Polymer* **2018**, *10*(1178), 1.
[21] X. Meng, V. Bocharova, H. Tekinalp, S. Cheng, A. Kisliuk, A. P. Sokolov, V. Kunc, W. H. Peter, S. Ozcan, *Mater. Des.* **2018**, *139*, 188.
[22] K. Oksman, Y. Aitomäki, A. P. Mathew, G. Siqueira, Q. Zhou, S. Butylina, S. Tanpichai, X. Zhou, S. Hooshmand, *Compos. Part A* **2016**, *83*, 2.
[23] X. Wang, Y. Jia, Z. Liu, J. Miao, *Polymer* **2018**, *10,*1013.
[24] R. Banerjee, S. Sinha Ray, *Polym. Eng. Sci.* **2021**, *61*, 617.
[25] E. Sabau, A. Popescu, C. Vilau, *MATEC Web Conf.*, **2017**, *137*, 1.
[26] Y. Zhao, Y. Chen, Y. Zhou, *Mater. Des.*, **2019**, *181*, 1.
[27] I. Sadrehaghighi, *CFD Open Ser.* **2020**, *139*, 1. https://doi.org/10.13140/RG.2.2.25026.94404
[28] M. Jawaid, M. Thariq, N. Saba, Modelling of damage processes in biocomposites, fibre-reinforced composites and hybrid composites. in *Woodhead Publishing Series in Composites Science and Engineering* **2019**, p. 153.
[29] M. Nurhaniza, M. Ariffin, A. Ali, F. Mustapha, W. Noraini, *IOP Conf. Ser. Mater. Sci. Eng.* n. 11 (012010) **2010**.
[30] M. Guimarães Junior, F. G. Teixeira, G. H. D. Tonoli, *Cellulose* **2018**, *25*, 1823.
[31] G. H. D. Tonoli, K. M. Holtman, G. Glenn, A. S. Fonseca, D. Wood, T. Williams, V. A. Sa, L. Torres, A. Klamczynski, W. J. Orts, *Cellulose* **2016**, *23*, 1239.
[32] I. Siró, D. Plackett, *Cellulose* **2010**, *17*, 459.
[33] S. Nam, A. D. French, B. D. Condon, M. Concha, *Carbohydr. Polym.* **2016**, *135*, 1.
[34] A. D. French, *Cellulose* **2014**, *21*, 885.
[35] J. Xie, C. Y. Hse, C. F. de Hoop, T. Hu, J. Qi, T. F. Shupe, *Carbohydr. Polym.* **2016**, *151*, 725.
[36] C. Yang, X. Tian, D. Li, Y. Cao, F. Zhao, C. Shi, *J. Mater. Process. Technol.* **2017**, *248*, 1.
[37] L. E. Silva, A. A. dos Santos, L. Torres, Z. McCaffrey, A. Klamczynski, G. Glenn, A. R. Sena Neto, D. Wood, T. Williams, W. Orts, R. A. P. Damásio, G. H. D. Tonoli, *Carbohydr. Polym.* **2021**, *252*, 117165.
[38] P. Patel, V. Chaudhary, K. Patel, P. Gohil, *Int. J. Appl. Eng. Res.* **2018**, *13*(10), 7455.
[39] V. Mishra,, G. Singh, C. Yadav, V. Karar, C. Prakash, S. Singh, *J. Thermoplast. Compos. Mater.* **2019**, *34*, 557.

How to cite this article: E. Zambaldi, R. R. Magalhães, M. C. Dias, L. M. Mendes, G. H. D. Tonoli, *Polym. Eng. Sci.* **2022**, *62*(12), 4043. https://doi.org/10.1002/pen.26165